

BEAM ELECTRONS AS A SOURCE OF H α FLARE RIBBONS

MALCOLM DRUETT*
Northumbria University
Newcastle upon Tyne
NE1 8ST, United Kingdom
malcolm.druett@northumbria.ac.uk

EAMON SCULLION
Northumbria University
Newcastle upon Tyne
NE1 8ST, United Kingdom

VALENTINA ZHARKOVA
Northumbria University
Newcastle upon Tyne
NE1 8ST, United Kingdom

SARAH MATTHEWS
Mullard Space Science Laboratory - University College London
Holmbury St. Mary, Dorking
Surrey, RH5 6NT, United Kingdom

SERGEI ZHARKOV
Hull University
Kingston upon Hull,
East Yorkshire, HU8 5ST, United Kingdom

LUC ROUPPE VAN DER VOORT
Institute of Theoretical Astrophysics
University of Oslo, P.O. Box 1029
Blindern, NO-0315, Oslo, Norway

ABSTRACT

From early 80s the observations of solar flare onsets show rapid increases of hard and soft X-rays, ultra-violet emission with large Doppler blue shifts associated with plasma upflows (with velocities up to 1000 km·s⁻¹) and H α hydrogen emission with red shifts up to 1-4 Å (downward velocities up to 50-200 km·s⁻¹). Modern radiative hydrodynamic models account well for blue-shifted emission but struggle to reproduce closely the red-shifted H α lines. Here we present the first joint hydrodynamic and radiative model showing that during first seconds of beam injection the effects caused by beam electrons can reproduce H α line profiles with large red-shifts corresponding to a downward velocity of 45-50 km·s⁻¹ and matching closely those observed in C1.5 flare with Swedish Solar Telescope. The model also accounts closely for timing and magnitude (93 km·s⁻¹) of upward motion to the corona observed 29 s after the event onset in 171 Å by the Atmospheric Imaging Assembly/ Solar Dynamics Observatory.

Keywords: Sun: chromosphere - Sun: flares - stars: flare - electron beam - hydrodynamics - radiation

mechanisms: non-thermal - radiative transfer - line: formation - line: profiles - techniques:
imaging spectroscopy

1. INTRODUCTION

Complex processes of plasma heating in solar flares can be effectively diagnosed from the increase of intensities of hard X-ray (HXR) emission combined with soft X-ray (SXR), extreme ultra-violet (EUV) and ultra-violet (UV) emission with blue-shifts reported from the early space observations^{1,2}. Flare dynamics in the lower atmosphere can be derived from observations of optical lines and, in particular, hydrogen H α line 6563 Å emission with red shifts^{3,4,5,6,7,8,9}. Further space missions uncovered details of this increase in coronal line intensities with upward velocities reaching 1000 km·s⁻¹^{13,4,10,11,5,12,6,13,14}. Often flares show SXR emission of highly ionised ions of FeXXIV or even FeXXV^{15,16}, which can be only produced by non-thermal processes¹⁷ linked to energetic particles.

Observations of flare emission with blue-shifts in coronal lines and red-shifts in chromospheric lines were interpreted by hydrodynamic (HD) responses of flaring atmospheres to heating by particle beams injected from the top and precipitating to lower atmospheric levels^{18,19,20,21,22}. There are three types of hydrodynamic models defined by their initial conditions, from which heating starts: *type 1* uses the quiet Sun chromosphere^{18,19,20,23} (in Lagrangian coordinates), which is converted by electron beam heating into a flaring atmosphere with its own corona, transition region and chromosphere; *type 2* uses a pre-heated flaring atmosphere comprising of semi-empirical model VAL F²⁴ in the chromosphere and the quiet Sun (QS) corona attached above the transition region in Lagrangian²¹ or linear^{22,25} coordinates, which is also heated by precipitating beam electrons; *type 3* uses an isotropic atmosphere evenly heated over a linear depth by some unspecified agents²⁶.

There are three types of heating function: *H1* - by beam electrons in Coulomb collisions with electron density derived from a continuity equation approach (CEA)^{18,23,27}; *H2* - by beam electrons in Coulomb collisions with density derived from a flux conservation equation (FCE)^{20,21,22,28}, which has a serious (infinity) limitation^{29,30} at the stopping depths in the chromosphere for electrons with the lower cutoff energy; *H3* - by unspecified agents with equal energy deposition per volume at any depths^{14,26}. Heating by particle beams is considered to be either impulsive of 5-10 s^{18,21,22,23}, or prolonged (30-300 s)^{14,19,20,25,26} accounting for different types of flaring events.

The cooling in all hydrodynamic models is provided by radiation from the corona and transition regions, calculated in optically thin emission for the solar abundances³¹. The additional cooling by hydrogen line emission in the chromosphere is calculated by solving radiative transfer equations^{21,22} or by adding hydrogen radiative losses for relevant beam parameters as arrays to the cooling function²³. A hydrodynamic timescale (10-100 s)^{32,33} is much longer compared to a radiative timescale (0.3 s)^{32,34} that supports a consequential use of hydrodynamic and radiative models.

Heating of the QS chromosphere by beam electrons (HD model type 1)^{18,19,23} is shown to sweep plasma to lower atmosphere, forming a flaring atmosphere with the new corona, transition region and chromosphere. This sweeping is followed by the plasma evaporation back to the corona combined with formation of a low-temperature condensation in the chromosphere moving as a shock to the photosphere. A hydrodynamic heating in the other two types of models (preheated and isotropic) results in chromospheric plasma evaporation without sweeping, combined with the shock moving downwards to the lower atmosphere with smaller velocities^{14,21,22,25,26}.

Most HD models^{14,18,20,21,22,25,26} account quite well for evaporation (upward) velocities and intensities of EUV emission. However, types 2 and 3 models are less successful in interpreting the red-shifted H α line profiles^{7,8,9,35}. Earlier calculations of H α line profiles^{36,37,38} carried out for pre-heated hydrodynamic atmospheres²¹, with heating function by Nagai & Emslie²⁰, showed the simulated profiles with blue-shifts, contrary to the red ones observed^{7,8,9,35}. These discrepancies were previously attributed to a complex geometric multi-thread structure of flares^{36,37,38}.

The advances in space and ground-based instruments with high spatial and temporal resolution (IRIS³⁹, the Atmospheric Imaging Assembly (AIA) aboard on the Solar Dynamic Observatory (SDO)⁴⁰ and notably the CRisp Imaging Spectro-Polarimeter⁴¹ located at the Swedish 1-m Solar Telescope (SST)^{42,43}) helped to eliminate some effects of spatial inhomogeneities in flaring regions emitting H α lines^{22,44,45,46,47}. Rubio da Costa et al.⁴⁷ reported simulated H α line profiles with a small red-shift (about 15 km·s⁻¹) at a flare onset and larger blue-shifts at 52 s later. However, this model still cannot explain the H α line observations^{7,8,35} with larger red-shifts taken at the flare onsets.

The radiative models describing hydrogen emission in flares utilise the effects of electron beams in two ways: *via heating of the ambient plasma* by beam electrons as considered in HD models and *via non-thermal ionisation and excitation* of hydrogen atoms by beam electrons for a flux conservation approach (FCA)⁴⁸ and for a continuity equation approach (CEA)^{27,49}. The heating and non-thermal excitation and ionisation rates of hydrogen atoms are significantly affected by the approaches used for particle kinetics, producing in FCA smaller electron numbers at chromospheric

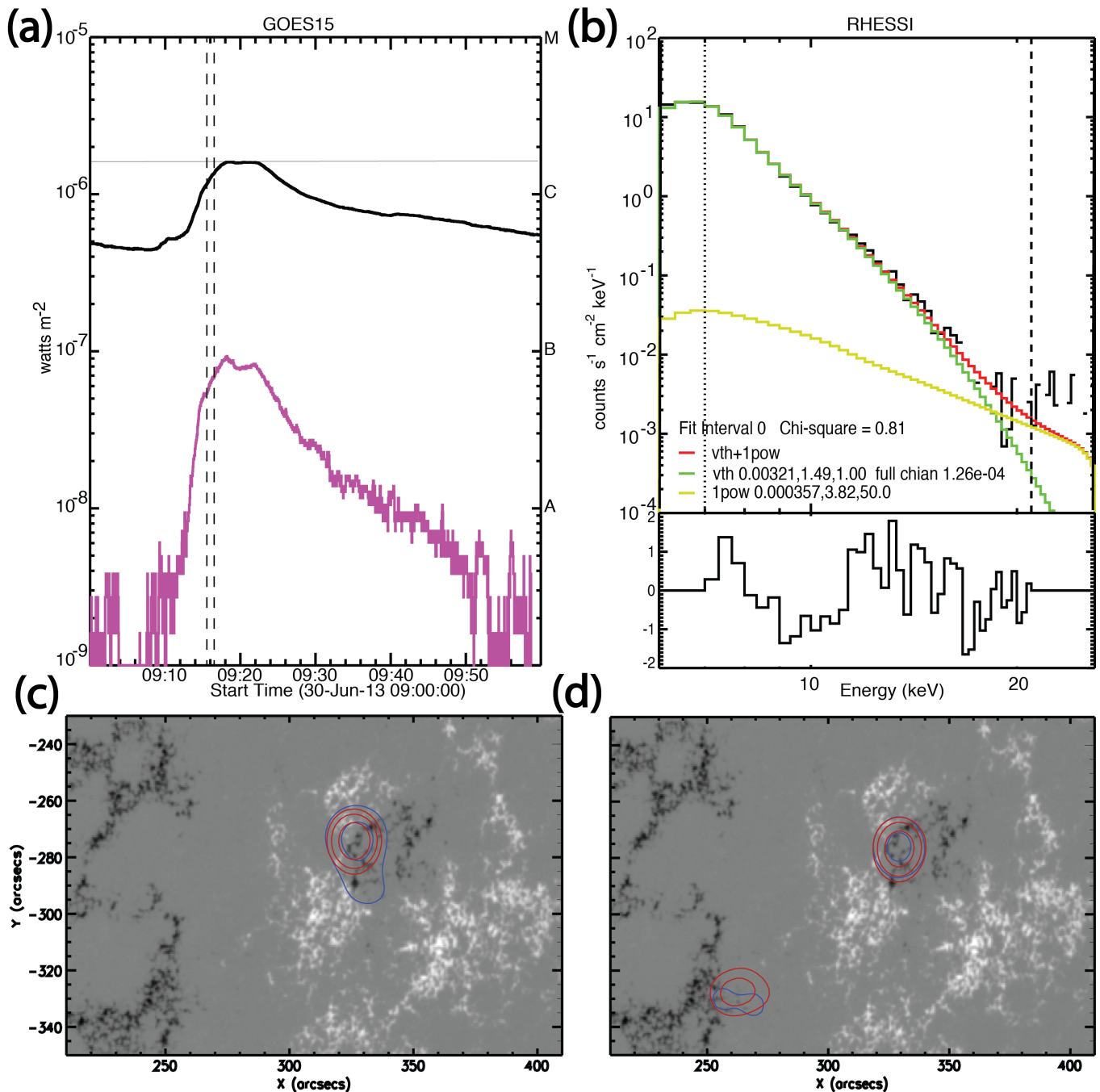


Figure 1. The active region topology and HXR emission. (a) The GOES X-Ray light curves of the flare in the 1-8 Å (black) and 0.5-4.0 Å (magenta) channels. The vertical dashed lines correspond to the time interval of the RHESSI spectrum in event 2. (b) RHESSI photon flux spectrum for event 2 with residuals derived with CLEAN in the 20 s interval around the time of H α emission for thermal (green line) plus single power-law (yellow line) components, giving the total (magenta line). HXR emission is mostly of thermal nature with a small non-thermal component (see for details the current section and 'Methods section: Reduction of H α line emission') with the parameters: spectral index about 3.8 and initial energy flux can be a factor (0.7-3) of $F_0 = 10^{10} \text{ erg}\cdot\text{cm}^{-2}\cdot\text{s}^{-1}$. (c) The HXR emission contours appearing in event 1 (top) and event 2 (Bottom, blue contour) coinciding with the times of the observations of H α kernels with red-shifts in the ribbon (09:16 UT). These are overlaid onto the HMI magnetogram. The response in the 5-12 keV channel is shown using red contours, and the response in the 12-25 keV channel with blue. (d) HXR emission overlaid on the HMI magnetogram appearing with the event 3 occurring ~ 4 minutes later (09:20 UT), during the maximum in GOES light curve.

levels compared to CEA. This occurs because of the electron number truncation in FCA at the upper chromosphere^{29,30}, before a stopping depth of lower energy electrons, in order to avoid the infinite heating²⁹. This, in turn, shifts to the upper chromospheric depths the effect of beam electrons on hydrogen emission in FCA.

The CEA provides very smooth distributions of beam electrons at all precipitation depths, with maximum heating occurring in the chromosphere at the stopping depth of electrons with a lower cutoff energy²⁷. This heating leads to formation of hydrodynamic shocks in the middle chromosphere where the H α line cores are formed, contrary to the hydrodynamic models type 2^{21,22} using FCA where this shock is formed in the upper chromosphere. Therefore, current radiative hydrodynamic models of type 2 and 3 cannot explain the red-shifted H α line profiles observed at flare onsets reported since early 80s.

In this paper we confirm the earlier observations^{7,8,35} by presenting H α line profiles with strong red shifts recorded using SST for a flaring event onset in a C1.5 flare. These profiles are interpreted with a simultaneous hydrodynamic model type 1²³ and full non-LTE (NLTE) radiative model for 5 level plus continuum hydrogen atoms (model HYDRO2GEN) by considering hydrogen non-thermal excitation and ionisation rates by beam electrons⁴⁹.

2. RESULTS

2.1. Active region topology and HXR emission

The C1.5 class flare occurred on 30th June 2013 in the active region (AR) 11778 during the time 09:11-09:27 UT, as per the GOES light curve in the 1.0-8.0 Å channel (Fig.1a: black line, with peak indicated by the grey horizontal line). The flare originated in a complex configuration of magnetic field with the opposite polarity connected to another active region located in the south east (Figs.1c and d). The initial flare started at 09:13:54 UT (event 1) in the north-east location of the negative polarity region of the AR11778 (Fig.1c).

At 09:15:54 UT it continued in the south-west location of the same region (event 2) (Fig.1c) where the H α ribbons were formed and the line profiles observed. A few minutes later HXR emission appeared at the location of the south east active region (event 3) (Fig.1d). The GOES light curves include the contributions from all three events of this active region. Event 2 (Fig.1d) contributes to this light curve at the times indicated between the vertical lines in Fig.1a. The data from the Helioseismic and Magnetic Imager (HMI) did not detect any sunquakes⁵⁰ in these events.

Fig.1b displays the HXR photon spectrum for event 2 measured by RHESSI with detectors 4, 5, and 9. The spectrum was fitted from 09:15:54 to 09:16:14 UT over the energy range 7 to 21 keV using Object Spectral Executive (OSPEX) and thermal (green line) plus single power-law (yellow line) components, giving the total (magenta line). The background period was 09:38:40 to 09:40:56 UT. The photon spectrum for event 2 can be also fitted by a thermal function only with the similar accuracy (χ^2). This indicates that HXR emission in the vicinity of event 2 has a strong thermal component related to a difference in spatial resolution for HXR and H α observations (see methods section 'Reduction of H α line emission'). For this reason, the HXR energy spectrum presented in Fig.1b) is for a demonstration only of a weak non-thermal component with spectral index of 3.8 and a lower cutoff energy of about 7-10 keV.

The HXR contour images in Figs.1c and d were made using the CLEAN algorithm and detectors 3 to 8 with 20 s integration times. The contour levels in 6-12 keV (red) and 12-25 keV (blue) are at 30%, 50%, and 70% of the maximum intensity, covering the area 6-8 pixels for the latter. The initial energy flux for event 2 was about 10^{26} erg.s⁻¹. The range of initial energy fluxes F_0 for this event 2 is discussed in the methods section 'Reduction of H α line emission'.

2.2. H α line and coronal jet images

H α images. The H α line observation sequence occurred from 09:15.54 UT to 10:17:18 UT and was carried out by SST using the CRisp Imaging Spectro-Polarimeter (CRISP)⁴². CRISP is especially suited for spectroscopic imaging of the chromosphere in the popular H α line (6562.8 Å), being equipped with three high-speed, low-noise CCD cameras that operate at a frame rate of 36 fps. The C1.5 class flare under investigation was captured in H α line within the CRISP Field-of-View (FOV) of 55×55'' centred at heliocentric coordinates [323.4'', -287.9''] (see Fig.2a). We refer to methods section 'Reduction of H α line emission' for a description of the reduction technique used for the CRISP data.

Coronal jet images. The images obtained by AIA instrument aboard on the Solar Dynamic Observatory (SDO)⁴⁰ were used for the background in Fig.2 to locate the H α ribbons. To achieve sub-AIA pixel accuracy in the temporal and spatial co-alignment of CRISP images with AIA, the photospheric bright points common to both FOV were cross-correlated. The AIA images (Fig.2b) for the hotter channels (i.e. transition region - He II 304 Å; Corona - Fe XII 171 Å; Flaring/hot Corona - Fe XXIII 94 Å) were reduced and aligned to 1700 Å, via the *aia_prep* routine in SolarSoft (IDL). Subsequent images in all AIA channels were de-rotated to the CRISP start time (see Fig.2). The SST telescope turret continually tracked the starting target. Therefore, throughout the observation the CRISP image sequences are excellently co-aligned with AIA and RHESSI images.

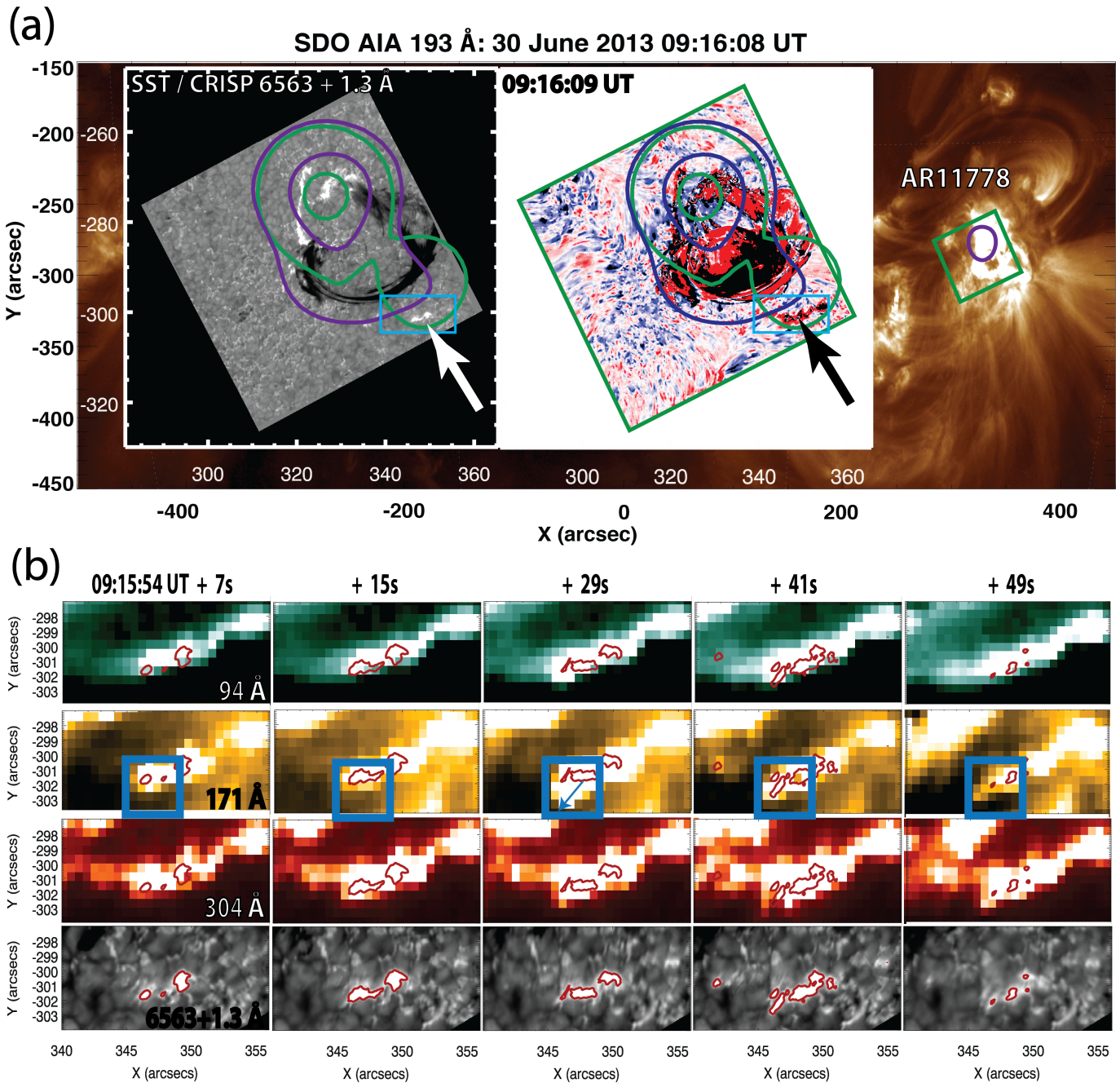


Figure 2. Observations with AIA. (a) *Background:* A context image for the observation in AIA 193 Å overlaid with the CRISP FOV outlined in green within AR11778. *Inset left:* The co-temporal (09:16:09 UT) CRISP image in the H α line far red wing reveals bright flare ribbons point to by the white arrow for event 2 that are co-spatial within RHESSI imaging contours in 6-12 keV (green) and 12-25 keV (purple). *Inset right:* The H α dopplergram for the 33 pt. spectral scan per pixel, containing blue/red-shifted motions marked by the relevant colour presented in the range of ± 20 km \cdot s $^{-1}$. The blue boxes in the insets (a) highlight the section of the ribbon formation in event 2, which is displayed in panel (b). (b) The image sequence describing evolution of the ribbon in the AIA 94 Å, 171 Å and 304 Å channels from top to bottom, respectively. These are co-spatial and co-temporal with the bright ribbon features (contoured in red), in the H α far red-wing images of +1.3 Å (bottom panel). The 171 Å channel reveals a bright jet-like protrusion (within the blue boxed region) that appears to form between the time frames 09:15:54 UT +15 s and +29 s (corresponding to 93 km \cdot s $^{-1}$) in the direction of the blue arrow and disappears by the time frame +49 s.

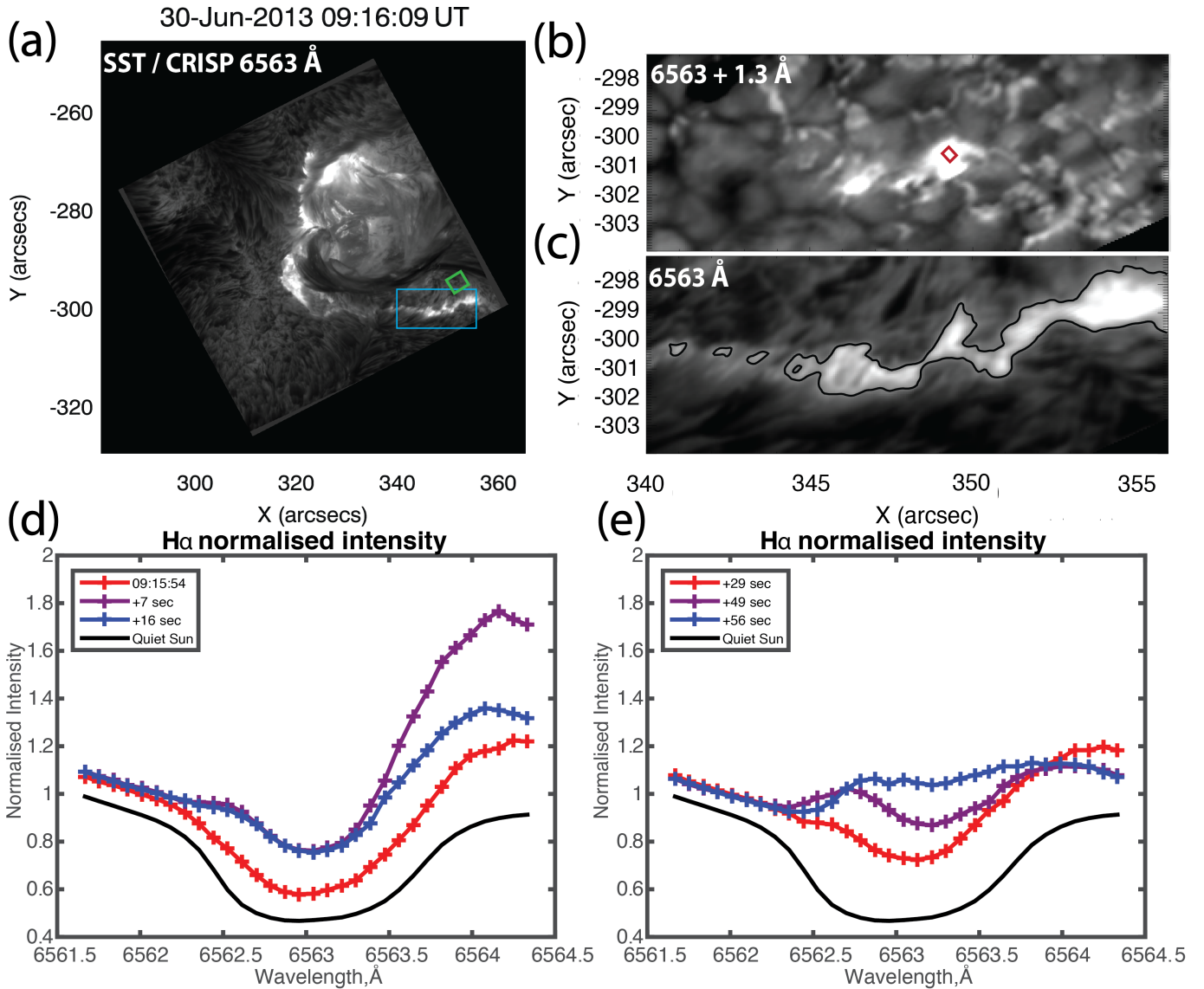


Figure 3. H α line profile observations using SST. (a) The CRISP H α line core image (6563Å) with a blue box outlining the part of the flare ribbon under investigation. The green box corresponds to the pixels selected to construct the average quiet Sun spectral profiles, i.e. close to the ribbon formation and free of any activity, within the time interval of the ribbon formation. (b) The corresponding FOV for the H α far red wing intensity at +1.3 Å, with a red box corresponding to the region where the spectral profiles of interest are extracted. (c) The contoured ribbons of the H α line core image for the blue box region is presented. (d) The averaged and normalized H α spectral line profiles, determined from the red box pixels, are presented for time intervals corresponding to the 1st (09:15:54 UT: red solid line), the 2nd (+7 s: purple solid line) and the 3rd (+16 s: blue solid line) time frames. The H α line profiles display exceptionally strong red-shifts. (e) The averaged and normalized H α spectral line profiles for significantly later time frames corresponding to +29 s (red solid line), +49 s (purple solid line) and +56 s (blue solid line) when there were no longer strong red-shifts but rather core emission with peaks in both blue and red near wings. The black solid lines describes the averaged QS background H α profile, deduced from the region defined by the green box in (a). Intensities were normalised against the background levels using the QS intensity of 9890 counts per pixel at 6561.7 Å as a reference.

2.3. H α -line profiles

The CRISP observation of event 2 (see 'Active Region topology and HXR emission' and Fig.1) began at 09:15:54 UT, just before the peak of flux in the GOES light curve produced by all three events. The H α line emission was subjected to data reduction and normalisation (see methods section 'Reduction of H α line emission'). Fig.3a shows the full CRISP field of view image in the H α line core (6563 Å) at 09:16:01 UT. The green box shows the 31×31 pixel square (1333 km²) used for the QS reference intensity, which had no interference from overlying structures during the relevant observational frames. The blue rectangle in Fig.3a displays the zoomed field of view used in panels b and c.

In Fig.3b we see the image taken in the red wing of $H\alpha$ at 6564.376 Å and Fig.3c show the line core. To assess the feature identified, data was extracted from a 5×5 pixel square (215 km^2), which contained the region of greatest red wing enhancement in the 09:16:01 UT frame. This kernel area is highlighted by the red square in Fig.3b.

The resulting $H\alpha$ line profiles are shown in Figs.3d and e. The CRISP observation captured the onset of a strong chromospheric downflow in the second ribbon area highlighted by the blue box in Fig.3a. The red wing enhancement started in the 09:15:54 UT frame (Fig.3d, red line), increased between 09:15:54 and 09:16:01 UT and peaked at 09:16:01 UT (Fig.3d, purple line), 7 s after the flare onset. Contrary to the symmetric $H\alpha$ line profile of the QS, the emission in the red wing exhibited a single-peaked profile (Fig.3d). This suggests that the peak can be attributed to a strong downflow in the chromosphere with Doppler velocity of $45\text{--}50\text{ km}\cdot\text{s}^{-1}$. This red wing enhancement was reduced 9 s later, while the core emission remained at a slightly raised level, compared to the QS (Fig.3d, blue line).

Throughout observations the blue wing had only a slightly raised intensity (without peaks) compared to the QS, in agreement with the wing intensity enhancement, or background level increase, appropriate to flares. 29 to 56 s later, the red wing enhancement was reduced towards the flare background level and the core intensity was increased for the times when the $H\alpha$ line was in emission (Fig.3e, blue line).

2.4. Hydrodynamic Response

The method for calculation of a hydrodynamic response of the flaring atmosphere to injection of power-law beam electrons is described in the methods section 'Hydrodynamic response to heating by an electron beam'.

Fig.4 shows plots of electron kinetic temperatures (a and d), macrovelocities (b and e) and plasma number densities (c and f) as functions of column depth calculated as a hydrodynamic response of the ambient plasma to injection of a power-law beam with the initial flux of $10^{10}\text{ erg}\cdot\text{cm}^{-2}\cdot\text{s}^{-1}$ (F10 model, left panels) and $3\times 10^{10}\text{ erg}\cdot\text{cm}^{-2}\cdot\text{s}^{-1}$ (3F10 model, right panels). The initial QS chromosphere density is indicated by the straight lines in Figs.4c and f. The flaring transition region is swept by the beam towards $3\times 10^{18}\text{ cm}^{-2}$ (F10 model) or $9\times 10^{18}\text{ cm}^{-2}$ (3F10 model), with the flaring chromosphere extending to $8\times 10^{19}\text{ cm}^{-2}$ (F10 model) or $2\times 10^{20}\text{ cm}^{-2}$ (3F10 model) followed by a flaring photosphere (Fig.4).

Temperatures in the flaring corona are strongly increased compared to the initial chromospheric temperature, with the magnitude scaled proportionally with the beam initial flux (compare Figs.4a and d). While the ambient density is significantly reduced from the initial QS chromospheric magnitude (10^{10} cm^{-3}) to $10^9\text{--}10^8\text{ cm}^{-3}$ to form the new corona of a flaring atmosphere¹⁸ (Fig.4c). These trends are similar to hydrodynamic models heated by electron beams with the same parameters reported by Fisher et al.²¹. The beams with moderate initial fluxes considered in this study do not heat the flaring corona to 10 MK (see Figs.4a and d) that is fully acceptable according to the statistical analysis of SXR emission in flares¹⁷. However, our hydrodynamic model heated by beams with the initial energy fluxes of $10^{11}\text{ erg}\cdot\text{cm}^{-2}\cdot\text{s}^{-1}$ or greater is proven to produce coronal temperatures of 10-20 MK^{18,23,51}.

The upward motion of a flaring plasma is reflected in the macrovelocity plots (Figs.4 b and e) showing evaporation of chromospheric plasma upwards to the newly formed corona at the column depths between 10^{17} and 10^{19} cm^{-2}) (Figs.4b, area below the box 1). This evaporation lasts, in general, for a few thousand seconds expanding upwards with increasing velocities even after the beam is stopped^{18,23}. The evaporation velocities range from a few tens of $\text{km}\cdot\text{s}^{-1}$ (at 1 s) to four hundred $\text{km}\cdot\text{s}^{-1}$ (at 20-100 s). The evaporation will increase the coronal density at later times (>3-5 min) as reported from observations^{14,19}.

At the same time, the beam energy deposition leads to formation of a low temperature condensation in the flaring chromosphere seconds after beam injection begins (Figs.4a, b, box 2) with a slightly increased temperature up to 10^4 K . This condensation moves as a shock towards the photosphere and interior⁵¹ with velocities from 30-35 $\text{km}\cdot\text{s}^{-1}$ (7F9 model) up to 50 $\text{km}\cdot\text{s}^{-1}$ (F10 model) (Fig.4b) and up to 90 $\text{km}\cdot\text{s}^{-1}$ (3F10 model) (Fig.4e). The density of this shock is about 10^{13} cm^{-3} (Fig.4c). This is different from the results of HD models of type 2 where the shock is formed at upper atmospheric depths^{14,22,25}, because of their different initial atmospheres and heating functions (see introduction section). However, both types of the hydrodynamic models (1 and 2) when simulated for a longer time (above 100 s considered in this paper) consistently show chromospheric plasma evaporation to the corona^{18,23,51} with similar velocities (up to 1000 $\text{km}\cdot\text{s}^{-1}$ ^{14,21} or up to 1500 $\text{km}\cdot\text{s}^{-1}$ ^{18,23,51}).

2.5. Probing hydrodynamic results with the AIA observations

In the considered HD model plasma evaporation (Figs.4a, b, box 1) (that can be called 'smooth evaporation'^{14,18,21}) starts from the first second of the beam injection and continues for 100 s (and above, not shown here). For F10 - 3F10 models it reaches velocities of 50-100 $\text{km}\cdot\text{s}^{-1}$ in the lower flaring corona and several hundred $\text{km}\cdot\text{s}^{-1}$ in the upper flaring corona (see Fig.4).

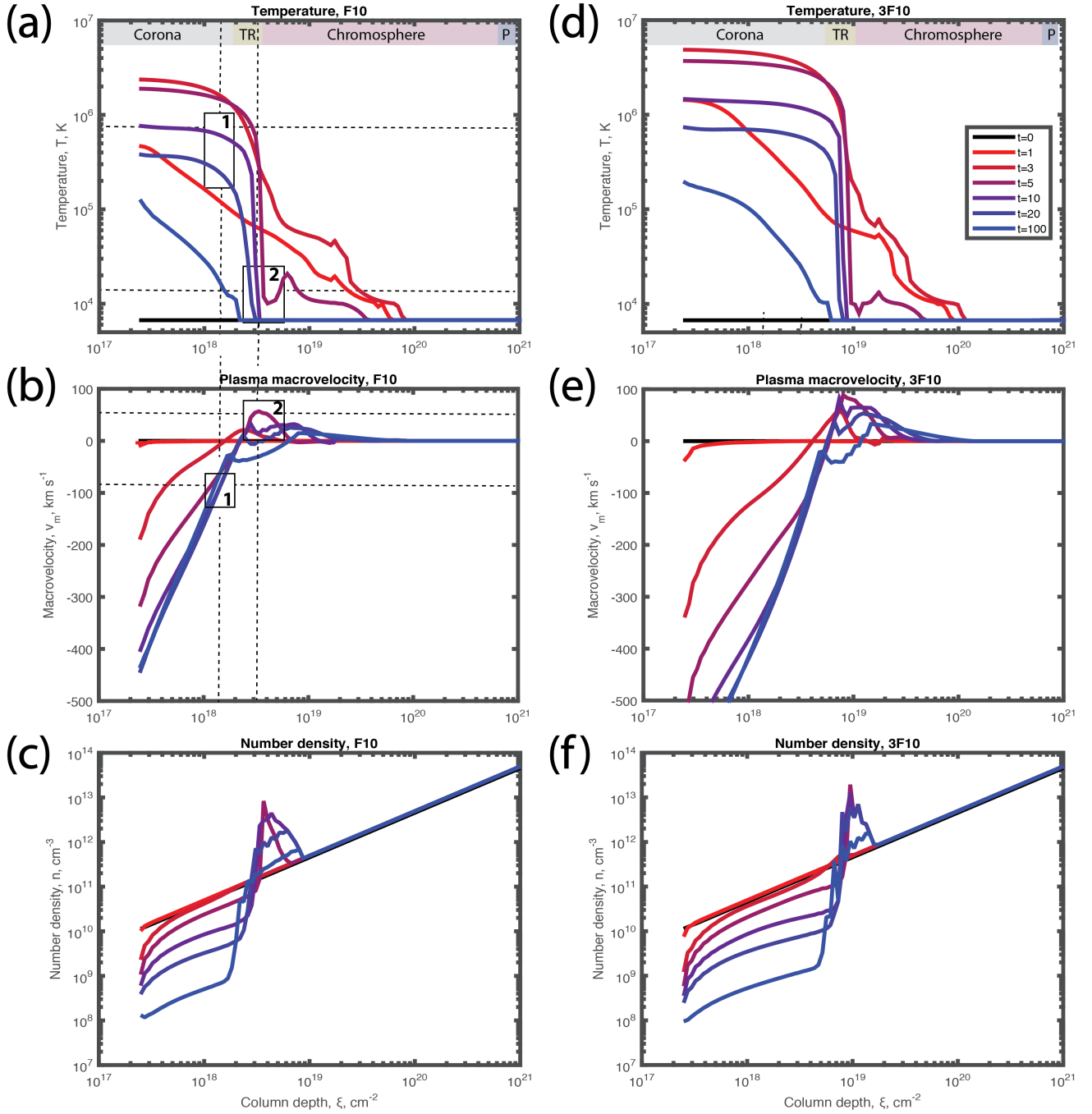


Figure 4. Simulated hydrodynamic responses. The simulated hydrodynamic responses of a flaring atmosphere to injection of a beam with the initial flux of 10^{10} $\text{erg}\cdot\text{cm}^{-2}\cdot\text{s}^{-1}$ (F10 model, left panels) and 3×10^{10} $\text{erg}\cdot\text{cm}^{-2}\cdot\text{s}^{-1}$ (3F10 model, right panels) following Zharkova & Zharkov²³ showing column depth dependencies of: (a and d) - the electron kinetic temperature, K, (b and e) - the plasma macrovelocity, $\text{km}\cdot\text{s}^{-1}$, and (c and f) - the plasma number density, cm^{-3} forming a flaring corona, chromosphere and photosphere (see the text for more details).

AIA observations of event 2 in 94 Å, 171 Å and 304 Å channels presented in Fig.2 have shown rather variable signatures. A bright, transient jet-like protrusion of plasma from the ribbon in the 171 Å AIA channel was detected between 15-29 s after the event onset, which appeared linked to the strong downflow regions in H α emission (red contours) (Fig.2b). At the same time, there are no jets seen in the 94 Å or 304 Å emission.

The jet velocity in 171 Å, measured 29 s after event 2 (beam injection) began, was 93 $\text{km}\cdot\text{s}^{-1}$. This was derived from the apparent motion of the jet within the AIA image set in the 171 Å channel. The error in measurements is sensitive to a pixel size (0.6''), reaching about ± 30 $\text{km}\cdot\text{s}^{-1}$ in the time frame of jet propagation. This estimation is accounted

for by a height of the box 1 within Fig.4b, which shows the macrovelocity within a range of 63-123 km·s⁻¹ centred at 93 km·s⁻¹. This velocity is close to other upflow observations of 100 km·s⁻¹ derived for flares with the similar beam parameters^{10,11}.

Comparison of the models presented in Figs.4a and b shows that the coronal temperature variations for 3F10 model would not account for the observed jet in the AIA 171 Å emission. However, the temperature profile evolution for F10 model between 5 and 100 s shown in Fig.4a, box 1, reveals that the plasma can be detectable in the temperature range of $\log T = 5.2$ to $\log T = 6.05$ at the depths of the low flaring corona. The 171 Å channel is the most sensitive to this range, compared to other available AIA channels (see methods section 'AIA line synthesis'). Moreover, the velocity range derived from the AIA 171 Å channel, averaged at 93 km·s⁻¹, also resembles closely for a given temperature range the predictions of F10 model of a hydrodynamic response to plasma heating by an electron beam shown in Fig.4a.

From the hydrodynamic simulations the response in 94 Å channel is expected to be rather weak. This is because the 94 Å emission is detected at a secondary sensitivity peak, at 1 MK relevant for the flaring corona in this event, and not at the main sensitivity peak of 10 MK (see Fig.6b, green line, methods section 'AIA line synthesis'). There was slightly increased signal in the 94 Å protrusion (Fig.3b, first row), which was most evident in 171 Å images (Fig.3b, second row, blue arrow).

The fact that the jet-like feature was seen only in the 171 Å channel and not in 304 Å or not clearly in 94 Å channel can be explained by a fast (tens of seconds) reduction of the plasma temperature and density in the newly formed flaring corona caused by radiative cooling, thermal conduction and plasma motion^{52,53}. Indeed, at the later times (20-30 s), after the beam is off, the coronal temperature was quickly reduced from two million to the sub-million Kelvin range (Fig.4a, box 1), and the plasma density was also reduced from the chromospheric (10^{10} cm⁻³) to coronal 10^9 cm⁻³ density (Fig.4c) (see methods section 'AIA line synthesis').

The cooling process in hydrodynamic model can quickly reduce the differential emission measure (DEM) of a flaring corona, as demonstrated in Fig.6 of Somov et al.¹⁸, allowing the coronal emissivity to reach the range matching the AIA sensitivity window (see methods section 'AIA line synthesis'). This made the plasma upflow detectable only in the AIA 171 Å passband at 29 s after the event onset when the coronal temperature in a flaring corona is dropped to the AIA range. Although, the coronal temperature in a flaring atmosphere at this time remains still too high for the intrusion to be clearly seen in the 304 Å passband, it can be observed later (>100 s) after further cooling.

2.6. Simulated radiative response in the H α line

The simulated H α line profiles were calculated for non-thermal excitation and ionisation by an electron beam with the initial fluxes of 10^{10} erg·cm⁻²·s⁻¹ (F10 model), 3×10^{10} erg·cm⁻²·s⁻¹ (3F10 model), representing an upper estimate of the flux and 7×10^9 erg·cm⁻²·s⁻¹ (7F9 model), representing a lower estimate with a beam spectral index of 4 (Figs.5a and c), as suggested by the RHESSI and tuned by H α observations (see methods section 'Reduction of H α line emission'). For calculation of H α line profiles the full NLTE problem for 5 levels plus continuum hydrogen atom was solved for the simulated hydrodynamic models using the approach described in the methods section 'Radiative transfer method'. The simulated profiles are normalised in the similar way to the observed profiles as described in the methods section 'Reduction of H α line emission'.

Non-thermal collisions between beam electrons and hydrogen atoms for all HD type 1 models cause excess excitation to the upper state ($n = 3$) of the H α line transition, quickly converting the H α spectral line from absorption into emission. The emission in the near wing wavelengths from the line centre have a lower optical depth and, thus, less absorption, resulting in the small intensity increase in the near wings (± 0.5 Å) (called 'horns') (see Fig.5). However, the main contribution of energetic beam electrons is to the strong ionisation of hydrogen atoms in a flaring atmosphere causing increase of their ionisation degree by orders of magnitude⁴⁹. This raises density of the ambient electrons, compared to the density expected from their kinetic temperature. This, in turn, produces a significant increase of H α line wing intensities owing to Stark's effect.

The radiative simulations clearly show that in the first seconds after the beam onset H α line profiles are dominated by non-thermal ionisation by the beam electrons and the downward motion of the shock (see Fig.4b, box 2). For this flaring event the beam has a relatively low initial energy flux about $0.7 - 3.0 \times 10^{10}$ erg·cm⁻²·s⁻¹ resulting in a moderate increase of the H α wing intensity (see Fig.5a). The horn in the near blue wing, about -0.5 Å from the central line wavelength (Fig.5a), is in a normal position to be caused by a radiative self-absorption as discussed above. However, the horn in the near red wing reveals a large increase of the intensity caused by a Doppler-shift of the emission wavelength caused by a downward movement of the hydrodynamic shock (see Fig.4b, box 2) growing from 35 km·s⁻¹ (7F9 model) up to 50 km·s⁻¹ (F10 model) or 90 km·s⁻¹ (for model 3F10) at the times of maximum beam deposition.

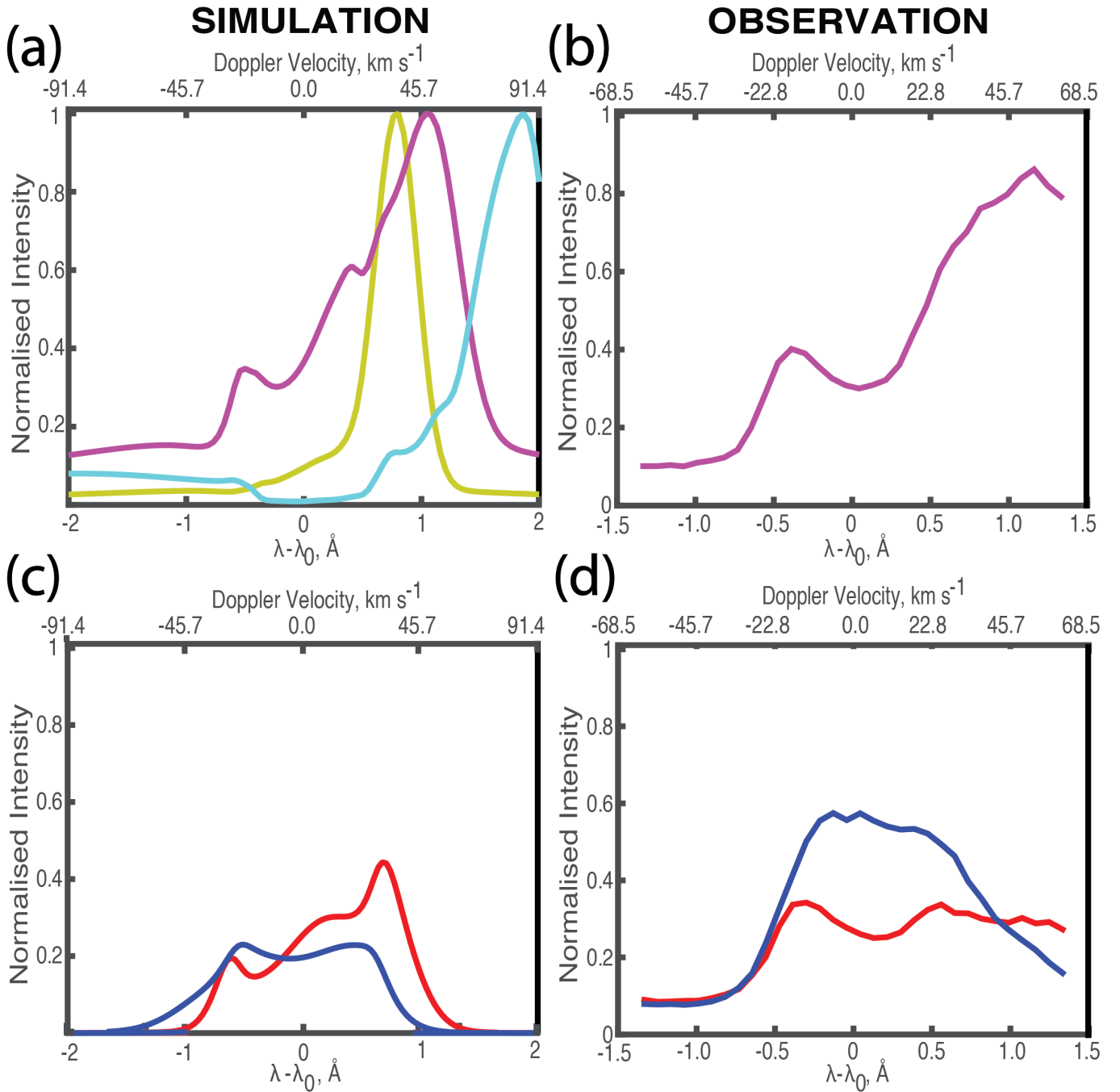


Figure 5. Simulated and observed $H\alpha$ line enhancements. (a) the synthetic $H\alpha$ line normalised intensity versus a distance ($\lambda - \lambda_0$), in \AA , from the $H\alpha$ line central wavelength, λ_0 ($\lambda_0 = 6563 \text{ \AA}$) taken from the simulation at +5 s after a beam onset for the F10 model (magenta line), the 3F10 model (cyan line) and a model with initial flux $7 \times 10^9 \text{ erg}\cdot\text{cm}^{-2}\cdot\text{s}^{-1}$ (7F9 model, yellow line) (b) the normalised background-subtracted $H\alpha$ profile observed +7 s after the ribbon onset in the event 2. (c) The $H\alpha$ line normalised intensity simulated for the F10 model at later times after the beam onset: +30 s (red solid line) and +70 s (blue solid line) and (d) the observed $H\alpha$ profiles at the similar times of +29 s (red solid line) and +56 s (blue solid line) after the event 2 onset.

When the beam is switched off, thermal heating and slow recombinations of the ambient electrons with hydrogen atoms become the main sources of sustaining hydrogen atoms' excitation and, thus, $H\alpha$ emission (see Fig.5c and d). One can see a decrease in the total intensity in the line compared to the intensity simulated during the beam injection (compare Figs.5a and c). There is also a decrease of the red wing intensity over the subsequent 60 s (Fig.5c). At later times in simulations, after the beam is off, $H\alpha$ emission profiles become standard thermal profiles, exhibiting after 70 s a small intensity enhancement in the blue horn (Fig.5c, blue line).

2.7. Comparison with $H\alpha$ line observations

The simulated $H\alpha$ line profiles were compared with the profiles observed by CRISP by averaging the emission over all the pixels in the red box of Fig.3b (with the QS background intensity subtracted) during the flare onset (Fig.5b) and over the next hundred seconds (Fig.5d). The simulation produces intensities of $H\alpha$ line emission from a flaring atmosphere within the spectral range ($\pm 3.0 \text{ \AA}$ from a central wavelength) that is broader than the observational range ($\pm 1.5 \text{ \AA}$). The simulated profiles are shown to $\pm 2 \text{ \AA}$ to demonstrate that the emission profile extended into a far red wing beyond the range (1.5 \AA) defined by the CRISP's current spectral filter.

The red-shift in the simulated $H\alpha$ line profile reaches a maximum at (or just after) 5 s of the electron beam onset when the downward velocity in hydrodynamic model is maximal (see Fig.4b, box 2). Only for the F10 model the shape of simulated $H\alpha$ line profile and a magnitude of the red shift is closely matched by the $H\alpha$ line profile observed by CRISP over the similar interval (7 s) after the event onset (Fig.5d), while the beam with lower or higher energy fluxes produce much smaller or much higher red shifts, than those observed.

The $H\alpha$ line core in model F10 is formed at depths of a HD shock, whose downward motion makes the line intensity red-shifted by around 1 \AA from the central wavelength ($\lambda_0 = 6563 \text{ \AA}$), corresponding to a Doppler velocity of $47 \text{ km}\cdot\text{s}^{-1}$ (Fig.5a). This is very close to the velocities of $45 - 50 \text{ km}\cdot\text{s}^{-1}$ derived from the observed profile (Fig.5b). Hence, we present the first successful interpretation of $H\alpha$ line red-shifted profiles observed at the onset of a flare that has been long overdue for the past three decades^{7,8}.

This comparison confirms that the observed red shift in $H\alpha$ line can be only caused by beam electrons with the initial flux close to $10^{10} \text{ erg}\cdot\text{cm}^{-2}\cdot\text{s}^{-1}$. Measuring Doppler shift of the emission outside of the horns of the $H\alpha$ line profile is an alternative method for determining the parameters of electron beam, allowing us to tune the estimations of initial energy flux derived from the low-resolution RHESSI data (see methods section 'Reduction of $H\alpha$ line emission').

3. DISCUSSION

In this study we presented multi-wavelength observations of a flaring event onset obtained with highest temporal and spatial resolution from CRISP/SST, AIA/SDO and RHESSI. The C1.5 class flare observed on 30 June 2013 in AR 11778 produced 3 flaring events, which contribute to its HXR and SXR light curves. The flaring event 2 produced two $H\alpha$ ribbons, in one of which $H\alpha$ line profiles were recorded in 5×5 pixels using CRISP/SST with the maximum downward velocity of $45 - 50 \text{ km}\cdot\text{s}^{-1}$. There are also plasma upflows of $93 \text{ km}\cdot\text{s}^{-1}$ observed in the 171 \AA AIA channel 29 s after the event onset, occurring just above the $H\alpha$ line ribbon with the downward motion.

These observations were successfully interpreted with the combined hydrodynamic and full NLTE radiative models (HYDRO2GEN) affected by power-law electron beams. The beam parameters for this event are estimated using the HXR photon spectrum observed by RHESSI and tuned with the high-resolution $H\alpha$ observations. Our simulations show that for this flaring event heating of flaring atmosphere by beam electrons in the HD model starts from the QS chromosphere, converting it into a flaring atmosphere with its own corona, transition region and chromosphere. Beam electrons quickly sweep the ambient plasma to deeper atmospheric layers causing, in turn, a fast upward motion of the swept plasma back to the corona and downward motion as hydrodynamic shocks^{18,23}.

The upward motion, which occurs from the first seconds after a beam onset, reflects the chromospheric evaporation caused by a hydrodynamic response of the flaring atmosphere to heating by electron beam. The chromospheric plasma in this upward motion for this flaring event is observed injected into a flaring corona 29 s after the event (or beam) onset that fits very well our hydrodynamic model and the sensitivity windows of the AIA in the different channels (94 \AA , 171 \AA and 304 \AA). The plasma jet becomes only visible in the AIA 171 \AA channel, at the times when the temperatures and densities of the flaring corona are reduced to the magnitudes detectable within this AIA passband.

Additional support to the proposed HYDRO2GEN model is provided from fitting the observed $H\alpha$ -line profiles with large red shifts by the simulated profiles obtained from a full NLTE approach applied to 1D flaring atmospheres being a HD response to electron beam heating. The $H\alpha$ line in flaring atmospheres is shown to be dominated by: *first*, an increase in the line wing intensities due to Stark's effect caused by non-thermal ionisation of the ambient hydrogen by beam electrons, and *second*, a hydrodynamic shock motion downward leading to large Doppler-shifts. The combination of these effects for this flaring event produces a big increase of the $H\alpha$ line intensity in the red wing at about 1 \AA from the line central wavelength, corresponding Doppler velocities of $45 - 50 \text{ km}\cdot\text{s}^{-1}$ derived from the observation. The latter is closely reproduced by the simulations only for the model F10, clearly restricting the initial energy flux of beam electrons capable of accounting for such the red shift. In addition, this close fit highlights a need to extend the spectral windows for observations of $H\alpha$ line dynamics in flaring atmospheres, which will allow capture of the profiles with large red shifts occurring in the first 100 s of a flaring event.

It should be noted that the ratio of red-to-blue wing intensities of the simulated $H\alpha$ line profile is slightly higher than in the observed profile, by a factor of 1.2. In addition, the wavelength of the central reversal (with the maximal absorption) in the simulated $H\alpha$ line profile at 5 s is slightly blue-shifted from the central wavelength, compared with the observations (compare Figs.5a and b). Such blue shifts of the central reversals in $H\alpha$ lines could be real as they were also observed by Ichimoto and Kurokawa⁷ for the profiles with strong red shifts (see their Fig.4a at 00:19:59 UT).

It appears that small blue (or red) shifts of the central reversals can reflect the overlying $H\alpha$ -line emission with strong upward (or downward) motions produced by different layers of a flaring event, so that their superposition could shift the central reversal emission towards the blue or red wing, accordingly⁷. There is also a possibility that the $H\alpha$ ribbon emission observed with SST occurred in a much smaller source size than the SST diffraction-limited resolution of 100 km in $H\alpha$. This could lead to over-smoothing, or averaging, of the observed $H\alpha$ line intensity over a larger area than the real emission comes from that causes the differences in the observed and simulated ratios of the red-to-blue horn intensities and the blue-shifted central intensity.

While this scenario is plausible, it still assumes that the observed red-to-blue intensity ratio is perfectly accurate, which may not be the case, given that we do not have infinite spatial resolution in the SST observations. Therefore, this outstanding issue cannot be fully reconciled beyond the limits of the current state-of-the-art SST observations and needs to be progressed with observations by the instruments with higher resolution, such as the Daniel K. Inouye Solar Telescope (DKIST)⁵⁴.

This study provides the first close interpretation of large red-shifted $H\alpha$ line observations of solar (and possibly stellar) flares indicating a need for broader spectral windows capable to fully capture the dynamics of flaring events.

4. METHODS

4.1. Reduction of $H\alpha$ -line emission

The $H\alpha$ observations consisted of equidistant scanning of 33 wavelength points from -1.38 \AA to $+1.38 \text{ \AA}$ about the $H\alpha$ line centre, resulting in an effective observation cadence of ~ 7.27 s. The image quality of the time series data significantly benefited from the correction of atmospheric distortions by the SST adaptive optics system⁴¹. Post-processing was applied to the data sets with the image restoration technique Multi-Object Multi-Frame Blind Deconvolution (MOMFBD)⁵⁵. Consequently, every image is close to the theoretical diffraction limit for the SST with respect to the observed wavelengths. We followed the standard procedures in the reduction pipeline for the CRISP data⁵⁶.

The mean $H\alpha$ profile intensities were taken in each of the 33 spectral positions of the QS and the flare kernel. Then the data was smoothed, to remove an instrumental spiking effect between adjacent spectral positions, by creating 32 interpolated spectral data points that are the mean of the two adjacent data points. Intensities were normalised against background levels using the QS average of 9890 counts per pixel at 6561.7 \AA as a reference. After 7 s, the kernel produced 10949 counts per pixel at the 6561.7 \AA spectral position and 17651 counts per pixel at the peak of the red-shifted intensity (6564.2 \AA).

From the CRISP $H\alpha$ red wing image taken at the time of greatest red wing enhancement (Fig.3b), a strong, transient enhancement at $6563+1.3\text{\AA}$ can be registered (depending on the emission level) in a range of 266-712 SST pixels with the resolution of $0.0592''$. Then a single RHESSI pixel ($2''\times 2''$) contains $33 \times 33 \approx 1100$ SST pixels. Since the RHESSI area was too big (6-8 pixels) and the resolution too low, the areas of $H\alpha$ flaring kernels for event 2 were used. Taking into account that $1'' = 725 \text{ km} = 7.25 \times 10^7 \text{ cm}$, the area is estimated to vary within $(0.3 - 1.4) \times 10^{16} \text{ cm}^2$. This leads to the estimation of initial energy flux of HXR emission for event 2 in the location of $H\alpha$ ribbon of about $F_0 \approx (0.7 - 3.0) \times 10^{10} \text{ erg}\cdot\text{cm}^{-2}\cdot\text{s}^{-1}$.

In order to derive the observed $H\alpha$ profile, we used a flaring kernel in ($5\times 5=$) 25 pixels of the SST event 2. The area covered by other ($1100-25=$) 1075 SST pixels (98% of a single RHESSI pixel) is the neighbouring area of this active region, which is not directly affected by this particular electron beam. This difference in the spatial resolutions of RHESSI and SST data also can explain a good fitting to thermal emission in the RHESSI data (coming from the pixels not associated with the $H\alpha$ enhancements). Therefore, the RHESSI data should be (and was) only used for estimating the order of magnitude of the beam flux, while the other means confirming the precise beam flux are required, e.g. from fitting of the $H\alpha$ line profiles described in the section 'Simulated radiative response in the $H\alpha$ line'.

4.2. Hydrodynamic response to heating by an electron beam

For physical conditions in a flaring atmosphere and with respect to findings from HXR emission in the section 'Active Region topology and HXR emission', we used the first part of HYDRO2GEN code simulating a 1D hydrodynamic response of the ambient plasma heated by a power law electron beam, adopted from Zharkova & Zharkov²³ (see their equations 3-6) following the model by Somov et al.¹⁸ updated with hydrogen radiative losses⁴⁹.

A hydrodynamic response of the ambient plasma in this event can also be caused by a high-energy thermal beam because the HXR flux derived from RHESSI can be equally well fit by the thermal curve (see the section 'Active Region topology and HXR emission'). However, as simulated by Somov et al.⁵⁷, the hydrodynamic response of a flaring atmosphere to a thermal beam is similar to that of a power-law beam, while raising the additional problem of thermal conductivity saturation. In order to avoid this problem, in our simulation for event 2, we chose to heat the flaring plasma by a power-law beam instead.

We consider a limited region of the QS chromosphere with column depths $\xi_{\min} \leq \xi \leq \xi_{\max}$, with $\xi_{\min} = 10^{17} \text{ cm}^{-2}$ corresponding to the QS transition region, followed by the chromosphere and at $\xi_{\max} = 10^{22} \text{ cm}^{-2}$ corresponding to the upper photosphere.

The initial QS chromosphere is assumed to be in hydrostatic equilibrium and the temperature is constant, e.g.

$$\begin{aligned} v(0, \xi) &= 0, \\ T_e(0, \xi) &= T_i(0, \xi) = T_0 = \text{const}, \end{aligned} \quad (1)$$

where the initial temperature T_0 was derived from the semi-empirical simulations²⁴ equal to 6700 K¹⁸.

The initial plasma density of the QS chromosphere is defined as follows

$$n(0, \xi) = n_{\min} + h_0^{-1}(\xi - \xi_{\min}), \quad (2)$$

where $n_{\min} = 10^{10} \text{ cm}^{-3}$ and h_0 is the height scale in a flaring loop:

$$h_0 = \frac{k[1 + x(T_0)]T_0}{\mu g_s}, \quad (3)$$

where k is Boltzmann's constant, x is the ionisation degree, g_s is the solar acceleration of gravity, $\mu = 1.44m_{\text{H}}$ is the average atom mass of the ambient plasma, m_{H} is the mass of hydrogen atom.

Let us neglect any heating fluxes at the top and bottom boundaries, e.g.

$$\frac{\partial T_{e,i}}{\partial \xi}(i, \xi_{\min}) = \frac{\partial T_{e,i}}{\partial \xi}(i, \xi_{\max}) = 0, \quad (4)$$

Let us also consider the upper boundary at the initial time to be a free surface at the presence of the external pressure p_{cor} described as:

$$p_{\text{cor}}(0, \xi_{\min}) = n_{\min}k[1 + x(T_0)]T_0. \quad (5)$$

The plasma velocity at the lower boundary is defined by the equation

$$\frac{\partial v}{\partial \xi}(t, \xi_{\max}) = 0. \quad (6)$$

The plasma is heated by an electron beam precipitating from the top boundary with the heating function derived from continuity equation²⁷. Plasma cooling is caused by the viscosity, or motion between electrons and ions¹⁸ and radiative cooling³¹ updated with the hydrogen radiative losses⁴⁹.

After solving this system of four partial differential equations with the initial and boundary conditions (1-6) for precipitating electron beam with given parameters (initial energy flux F_0 and spectral index γ) we obtain time-dependent distributions of electron T_e and ion T_i temperatures, ambient plasma density T and macrovelocities, v .

Heating by electron beam is found to sweep the plasma from the QS chromosphere towards deeper atmospheric levels converting the QS chromosphere into a flaring atmosphere with its own corona, transition region and chromosphere^{18,23}. This is different from the other hydrodynamic models (Type 2 and 3 from the first section), which use semi-empirical (pre-heated) flaring chromospheres VAL F²⁴ with the attached QS corona as the initial condition^{21,22}. Thus, they are skipping the phase of conversion of the QS chromosphere into a flaring corona, flaring transition region and flaring chromosphere. The pre-heated hydrodynamic models work perfectly well for flares with pre-flare events, while our model is more applicable for the initial flaring events without prior heating.

The parameters of an injected beam are selected close to the range of parameters of HXR emission derived from RHESSI for event 2 (see section 'Active Region topology and HXR emission'): a single power-law energy spectrum with a spectral index of about 4 based on a comparison of spectral indices using Fokker-Planck approach (see Fig.11 in⁵⁸), a lower cut-off energy of 7-10 KeV (from the total range 7-21 keV recorded by RHESSI). The limits of initial energy flux of beam electrons in event 2 was estimated from HXR emission utilising the areas of H α kernels because of strong contamination of HXR with thermal emission of the background corona owing to a much lower spatial resolution of the RHESSI (2") versus SST (0.06") pixels (Methods section 'Reduction of H α line emission').

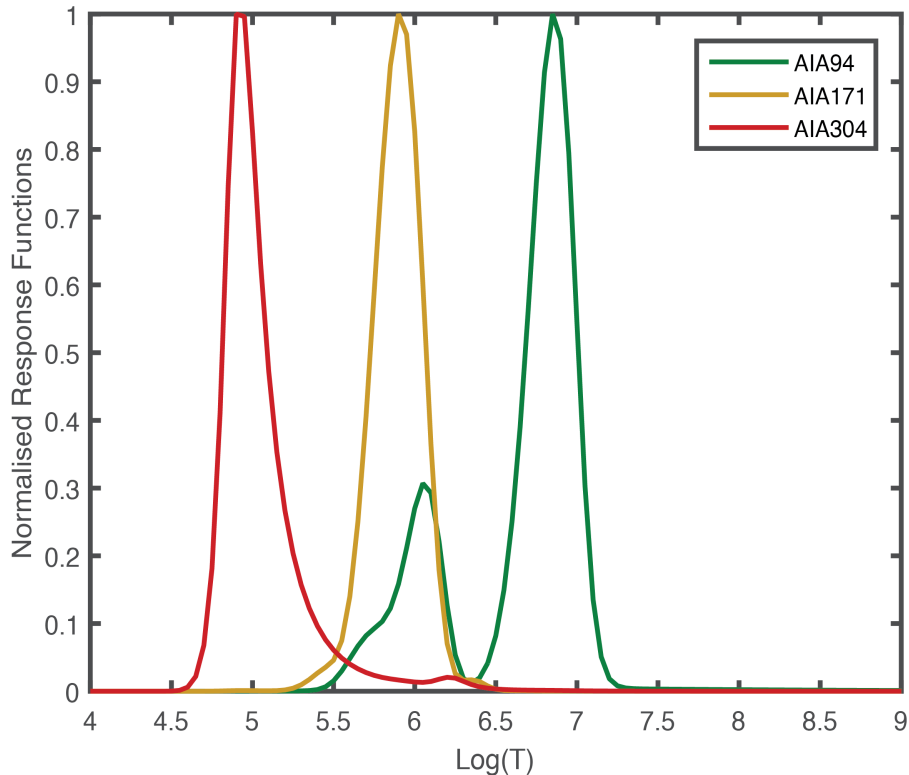


Figure 6. The normalised response functions of the AIA channels. The normalised response functions of the AIA 94 Å (green line), 171 Å (yellow line) and 304 Å (red line) channels plotted against \log_{10} of T (temperature). The AIA 94 Å channel has its largest sensitivity peak close to 10 MK but it is not limited in sensitivity to that specific temperature. It is shown in the green line that the AIA 94 Å channel has a secondary peak with maximum at the temperature of 1-2 MK.

Three hydrodynamic models were produced for heating by beam electrons with the initial energy fluxes covering the upper and lower estimates: $F_0 = 7 \times 10^{10}$ (7F9 model), $F_0 = 10^{10}$ $\text{erg}\cdot\text{cm}^{-2}\cdot\text{s}^{-1}$ (F10 model) and $F_0 = 3 \times 10^{10}$ $\text{erg}\cdot\text{cm}^{-2}\cdot\text{s}^{-1}$ (3F10 model). The duration of beam injection is chosen as 10 s to match the fast rise in $\text{H}\alpha$ emission. The initial energy flux of a beam varies as a triangular function in time, with maximum at five seconds²³. The NLTE simulations for these HD atmospheres (called HYDRO2GEN model) enabled to verify most applicable initial electron flux for the event 2 by comparing the observed $\text{H}\alpha$ profiles with the simulated ones (see Fig.5a and discussion).

4.3. AIA line synthesis

The HD models of type 1 presented in this paper include a flaring corona that is obtained from a conversion of the QS chromosphere, rather than having initially an inherent corona in HD models of type 2. Although, it should be noted that a large area covered by AIA pixels is the neighbouring corona, because given the difference in spatial resolutions of the AIA (0.6") and SST (0.06") pixels, the minimum area covered by a single AIA pixel includes $10 \times 10 = 100$ SST pixels. Within these, only 25 pixels contain $\text{H}\alpha$ emission while the other 75 pixels are, in fact, the neighbouring corona rather than the flaring event for which our hydrodynamic model is applicable. Therefore, our model does not intend to explain the contributions of any neighbouring coronal pixels to the emission of a flaring corona captured also by AIA, because our model certainly is not intended and does not solve the quiet coronal heating problem.

Each passband in the images from AIA detects plasmas with different emissivity defined by the local atmospheric temperature and density. The normalised instrumental response functions of the AIA channels are shown in Fig.6 plotted against \log_{10} of T (temperature) for the spectral lines of interest (94 Å, 171 Å and 304 Å). The AIA 94 Å channel has its largest sensitivity peak close to 10 MK combined with a secondary sensitivity peak close to the temperature of 1 MK (green line in Fig.6), i.e. it is sensitive to the flaring corona temperature peak (1-2 MK, see Fig.4a) in the flaring event 2 derived from the F10 model. We therefore expect to observe slightly enhanced emission from the source of the beam injection in the 94 Å channel above the observed background level, in addition to a strong enhancement in the 171 Å channel over the background level (see Fig.7a).

The intensity responses, I_i for each of the AIA channels i , were simulated following the AIA calibration method

described by Boerner et al.⁵⁹,

$$I_i = \int K_i(T(z))n_e^2(z)dz, \quad (7)$$

where $K_i(T)$ is the temperature response function for the AIA channel i ⁵⁹, shown in Fig.6, n_e is the electron density, and the integral is performed over the height z , of the model atmosphere.

Fig.7a shows the simulated (green line) and observed (green crosses) light curves for AIA 94 Å channel, and likewise, in yellow, the light curves for the AIA 171 Å channel. There is a small increase above the background levels in the observed AIA 94 Å emission (green crosses) during the first 20-30 s (Fig.7a). Due to the secondary sensitivity peak in AIA 94 Å, this flaring F10 model is capable of producing the AIA 94 Å enhancements on the order of $1 - 2 \times 10^2$ in intensity (DN units) (Fig.7a, green line) at the temperature of 1-2 MK, hence, confirming that 94Å emission is detectable from this model.

Most importantly, the F10 HD model leads to a much greater excess of intensity in the AIA 171 Å channel for some time during and after the beam injection (Fig.7a, yellow line), as observed (Fig.7a, yellow crosses). This AIA 171 Å enhancement should remain visible during the outflow (jet) process, and is indeed observed (see Fig.2b, blue arrow). The *simulated jet* travels at $\sim 90 \text{ km s}^{-1}$ and the *observed jet* traverses 3 pixels in the image space corresponding to $\sim 1500 \text{ km}$. Hence, the simulated jet would take $\sim 15-20 \text{ s}$ to appear 3 pixels from the $\text{H}\alpha$ kernel location in the observations (or later if travelling at some angle out of the plane of observation). So the simulation predicts that we should only expect to see the displacement of the jet after this time, in agreement with observations (Fig.2b, blue arrow).

The simulated light curves in the two channels were normalised to unity at their peak values (Fig.7b) and subtracted, in order to analyse the excess of the AIA171 Å enhancement relative to that in AIA 94 Å. This excess is plotted as a fraction of the enhancement in the AIA 171 Å channel in Fig.7c.

The enhancement in AIA 171 Å peaks during the beam injection phase (0-10 s) and decreases afterwards (Fig.7a). After 50 s the response in this channel has returned to background level (Fig.7a). Because the jet is observed away from the $\text{H}\alpha$ kernel location after 20 s and the AIA cadence is 12 s, the jet should only be visible in AIA 171 Å for 1-2 time frames according to the F10 model (as indicated by the FWHM line plotted in Fig.7b), which is indeed the case (Fig.2b).

Fig.7c and shows that at 30 s our model predicts a much greater enhancement over the AIA 171 Å background than over the AIA 94 Å background. Therefore, the F10 model predicts the presence of a jet, outflowing from the chromospheric source of beam heating, that is visible in AIA 171 Å and not AIA 94 Å at around 30 s. The fact that a jet is not observed in AIA 94 Å but only in AIA 171 Å (Fig.2b), adds further evidence to support the value of the flux used in the F10 model, because it places an upper boundary on the temperature, T , of the outflow, i.e. T is much less than 10 MK, and limited to 1-2 MK. At the same time, the jet is not observed in AIA 304 Å (Fig.2b) resulting in similar implications for the lower temperature. One can conclude that the jet must be also much hotter than 100,000 K (the sensitivity peak for the AIA 304 Å channel). This is why this jet is clearly observed in the AIA 171 Å channel.

4.4. Radiative transfer method

For the interpretation of hydrogen emission in flaring atmospheres defined by the hydrodynamic models discussed above we use the second part of HYDRO2GEN code utilising a full non-LTE approach for a 5 level plus continuum hydrogen model atom. Both radiative and collisional mechanisms of hydrogen activation and deactivation are considered for thermal and beam electrons, external and internal diffusive radiation, and three-body recombinations.

Here we consider hydrogen excitation and ionisation by beam electrons in addition to thermal ones, because only the non-thermal rates can explain the rapid (one second or so) increase of $\text{H}\alpha$ line emission in the core and wings. Thermal electrons, even with higher temperatures, cannot account for timing and shape of the observed $\text{H}\alpha$ line emission.

For non-thermal hydrogen excitation and ionisation rates by beam electrons the analytical formulae by Zharkova & Kobylinskii⁴⁹ were used, with the beam electron densities calculated from the continuity equation^{27,60}. Stimulated photo-excitation, de-excitation, and ionisation rates by external sources were taken from Zharkova & Kobylinskii⁶¹.

Steady state equations are considered for all the transitions in a 5 level plus continuum hydrogen atom model. For the lines and Lyman continuum, which are optically thick, the radiative transfer equations are solved in the integral form, as follows:

$$S(\tau) = \frac{\lambda}{2} \int_0^{\tau_0} K_1(|\tau - t|)S(t)dt + S^*(\tau), \quad (8)$$

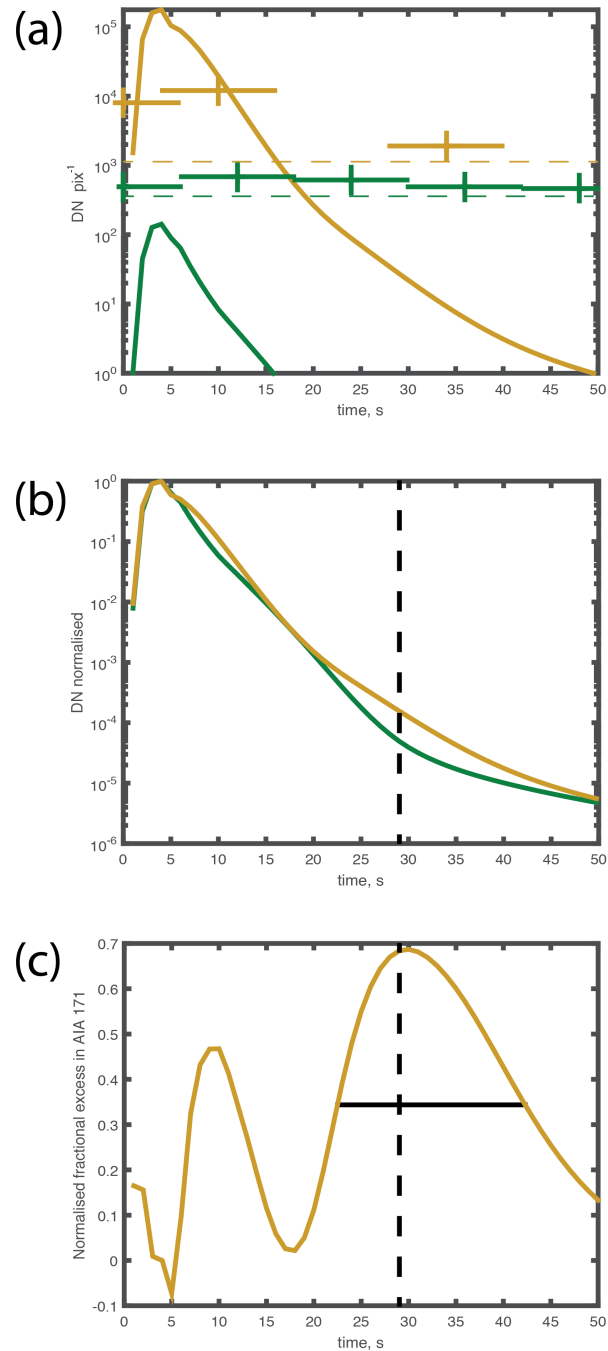


Figure 7. Simulated and observed AIA light curves. (a) The simulated light curves in the AIA 94 Å (green line) and 171 Å (yellow line) channels for contributions from the flaring corona, transition region and chromosphere. The simulation does not include background from the overlying upper corona or neighbouring corona. Observed values for the 94 Å (green crosses) and 171 Å (yellow crosses) channels including this background are shown. (b) The simulated profiles of the signals in AIA 94 Å (green line) and 171 Å (yellow line) above background. These profiles have been normalised to 1 at their peak values. The AIA 171 Å channel is particularly bright compared to the AIA 94 Å channel at around 30 s. (c) The normalised fractional excess in AIA 171 Å. The normalised light curves in panel b were subtracted to find the relative excess in the 171 Å channel. This excess is plotted as a fraction of the emission in the 171 Å channel at each instant. The full width half maximum (Horizontal black bar) indicates the times at which the jet is particularly bright in AIA 171 Å compared to AIA 94 Å, the vertical bar represents the maximum relative brightness at around 30 s.

where S is the source function for the line or continuum, τ is an optical depth in the line centre or the continuum head, λ is the survival probability of a scattered photon, and S^* is the initial source function, calculated without diffusive radiation. The integral was calculated over all the optical depths up to its maximum value for each different wavelength, τ_0 .

The kernel functions, K_1 , in the lines and Lyman continuum are given by the following equations:

$$\begin{aligned} K_1(|\tau|) &= F(T) \int_{\nu_{1c}}^{\infty} f_1 \nu^2 \exp\left[-\frac{h(\nu-\nu_{1c})}{kT}\right] E_1(|\tau|f_1) d\nu, & \text{Lyman continuum} \\ K_1(|\tau|) &= A \int_{-\infty}^{\infty} (\alpha(x))^2 E_1(|\tau|\alpha(x)) dx. & \text{Lines} \end{aligned} \quad (9)$$

$F(T)$ is a normalisation coefficient of the kernel functions for the Lyman continuum, and A is the one for the lines. T is the kinetic temperature of the plasma, ν is the frequency of the radiation and ν_{1c} the frequency in the Lyman continuum head. $E_1(x)$ is the exponential integral of the first kind. The absorption profiles in the lines, $\alpha(x)$, were taken in the form of a Voigt function, where x is a dimensionless wavelength measured in Doppler half widths from the line central wavelength. The effective Doppler half widths of spectral lines, $\Delta\nu_D$, defined by thermal motion of hydrogen atoms are calculated for the temperature profiles from the hydrodynamic model for every instant of beam injection by considering the contribution of the relevant Doppler widths from each layer weighed by the layer thickness. Turbulent velocities were included in the calculation of the Doppler half widths⁶², and were around $1 \text{ km}\cdot\text{s}^{-1}$ in the flaring chromosphere. At all depths this produced only a very small additional contribution to the Doppler half widths due to thermal velocities. For the Balmer lines Stark's effect, due to strong electric fields caused by ionisation of the ambient plasma, was also considered.

The absorption profile in the Lyman continuum, f_1 , is defined as follows:

$$f_1 = \left(\frac{\nu_{1c}}{\nu}\right)^3. \quad (10)$$

The radiative transfer and statistical equilibrium equations were solved together to define source functions in each atomic transition and ionisation degree of hydrogen atoms in the atmosphere at any given instant of a hydrodynamic response. The solutions of the radiative transfer equations (8) were found using the L2 approximation described by Ivanov & Serbin⁶³. The system of integro-algebraic, non-linear equations was solved iteratively until all the source functions are converged with the relative accuracy of 10^{-5} . Then the simulated $\text{H}\alpha$ line intensities are calculated from the relevant source function using Voigt's absorption profiles. For the ease of comparison with observations, the simulated profiles are normalised to the same units as the observed intensity.

4.5. Data availability

The datasets generated during and/or analysed during the current study are available from the corresponding author and valentina.zharkova@northumbria.ac.uk on a reasonable request.

REFERENCES

1. Doschek, G. A., Kreplin, R. W. & Feldman, U. High-resolution solar flare X-ray spectra. *ApJL* **233**, L157–L160 (1979).
2. Antonucci, E. *et al.* Impulsive phase of flares in soft X-ray emission. *SoPh* **78**, 107–123 (1982).
3. Zarro, D. M., Canfield, R. C., Metcalf, T. R. & Strong, K. T. Explosive plasma flows in a solar flare. *ApJ* **324**, 582–589 (1988).
4. Del Zanna, G. Flare lines in Hinode EIS spectra. *A&A* **481**, L69–L72 (2008).
5. Milligan, R. O. & Dennis, B. R. Velocity Characteristics of Evaporated Plasma Using Hinode/EUV Imaging Spectrometer. *ApJ* **699**, 968–975 (2009).
6. Graham, D. R. & Cauzzi, G. Temporal Evolution of Multiple Evaporating Ribbon Sources in a Solar Flare. *ApJL* **807**, L22 (2015).
7. Ichimoto, K. & Kurokawa, H. H-alpha red asymmetry of solar flares. *SoPh* **93**, 105–121 (1984).
8. Wuelser, J.-P. & Marti, H. High time resolution observations of H alpha line profiles during the impulsive phase of a solar flare. *ApJ* **341**, 1088–1096 (1989).
9. Canfield, R. C., Penn, M. J., Wulser, J.-P. & Kiplinger, A. L. H-alpha spectra of dynamic chromospheric processes in five well-observed X-ray flares. *ApJ* **363**, 318–325 (1990).
10. Milligan, R. O., Gallagher, P. T., Mathioudakis, M. & Keenan, F. P. Observational Evidence of Gentle Chromospheric Evaporation during the Impulsive Phase of a Solar Flare. *ApJL* **642**, L169–L171 (2006).
11. Milligan, R. O. *et al.* RHESSI and SOHO CDS Observations of Explosive Chromospheric Evaporation. *ApJL* **638**, L117–L120 (2006).

12. Ryan, D. F., O'Flannagain, A. M., Aschwanden, M. J. & Gallagher, P. T. The Compatibility of Flare Temperatures Observed with AIA, GOES, and RHESSI. *SoPh* **289**, 2547–2563 (2014).
13. Tian, H. *et al.* Temporal Evolution of Chromospheric Evaporation: Case Studies of the M1.1 Flare on 2014 September 6 and X1.6 Flare on 2014 September 10. *ApJ* **811**, 139 (2015).
14. Polito, V. *et al.* Simultaneous IRIS and Hinode/EIS Observations and Modelling of the 2014 October 27 X2.0 Class Flare. *ApJ* **816**, 89 (2016).
15. Porquet, D., Arnaud, M. & Decourchelle, A. Impacts of a power-law non-thermal electron tail on the ionization and recombination rates. *A&A* **373**, 1110–1124 (2001).
16. Kawate, T., Keenan, F. P. & Jess, D. B. Departure of High-temperature Iron Lines from the Equilibrium State in Flaring Solar Plasmas. *ApJ* **826**, 3 (2016).
17. Ryan, D. F. *et al.* The Thermal Properties of Solar Flares over Three Solar Cycles Using GOES X-Ray Observations. *ApJS* **202**, 11 (2012).
18. Somov, B. V., Spektor, A. R. & Syrovatskii, S. I. Hydrodynamic response of the solar chromosphere to an elementary flare burst. I - Heating by accelerated electrons. *SoPh* **73**, 145–155 (1981).
19. Duijveman, A., Somov, B. V. & Spektor, A. R. Evolution of a flaring loop after injection of energetic electrons. *SoPh* **88**, 257–273 (1983).
20. Nagai, F. & Emslie, A. G. Gas dynamics in the impulsive phase of solar flares. I Thick-target heating by nonthermal electrons. *ApJ* **279**, 896–908 (1984).
21. Fisher, G. H., Canfield, R. C. & McClymont, A. N. Flare loop radiative hydrodynamics. V - Response to thick-target heating. VI - Chromospheric evaporation due to heating by nonthermal electrons. VII - Dynamics of the thick-target heated chromosphere. *ApJ* **289**, 414–441 (1985).
22. Allred, J. C., Hawley, S. L., Abbett, W. P. & Carlsson, M. Radiative Hydrodynamic Models of the Optical and Ultraviolet Emission from Solar Flares. *ApJ* **630**, 573–586 (2005).
23. Zharkova, V. V. & Zharkov, S. I. On the Origin of Three Seismic Sources in the Proton-rich Flare of 2003 October 28. *ApJ* **664**, 573–585 (2007).
24. Vernazza, J. E., Avrett, E. H. & Loeser, R. Structure of the solar chromosphere. III - Models of the EUV brightness components of the quiet-sun. *ApJS* **45**, 635–725 (1981).
25. Kennedy, M. B., Milligan, R. O., Allred, J. C., Mathioudakis, M. & Keenan, F. P. Radiative hydrodynamic modelling and observations of the X-class solar flare on 2011 March 9. *A&A* **578**, A72 (2015).
26. Bradshaw, S. J. & Cargill, P. J. Explosive heating of low-density coronal plasma. *A&A* **458**, 987–995 (2006).
27. Syrovatskii, S. I. & Shmeleva, O. P. Heating of Plasma by High-Energy Electrons, and Nonthermal X-Ray Emission in Solar Flares. *Soviet Astronomy* **16**, 273–+ (1972).
28. Emslie, A. G. The collisional interaction of a beam of charged particles with a hydrogen target of arbitrary ionization level. *ApJ* **224**, 241–246 (1978).
29. Mauas, P. J. D. & Gómez, D. O. Fokker-Planck Description of Electron Beams in the Solar Chromosphere. *ApJ* **483**, 496–506 (1997).
30. Kontar, E. P. *et al.* Deducing Electron Properties from Hard X-ray Observations. *SSRv* **159**, 157, p.6, footnote (2011).
31. Cox, D. P. & Tucker, W. H. Ionization Equilibrium and Radiative Cooling of a Low-Density Plasma. *ApJ* **157**, 1157 (1969).
32. Shmeleva, O. P. & Syrovatskii, S. I. Distribution of Temperature and Emission Measure in a Steadily Heated Solar Atmosphere. *SoPh* **33**, 341–362 (1973).
33. McClymont, A. N. & Canfield, R. C. Flare loop radiative hydrodynamics. I - Basic methods. *ApJ* **265**, 483–506 (1983).
34. Somov, B. V. (ed.). *Cosmic Plasma Physics*, vol. 251 of *Astrophysics and Space Science Library* (2000).
35. Wuelsel, J.-P. *et al.* Multispectral observations of chromospheric evaporation in the 1991 November 15 X-class solar flare. *ApJ* **424**, 459–465 (1994).
36. Ricchiazzi, P. J. & Canfield, R. C. A static model of chromospheric heating in solar flares. *ApJ* **272**, 739–755 (1983).
37. Canfield, R. C., Gunkler, T. A. & Ricchiazzi, P. J. The H-alpha spectral signatures of solar flare nonthermal electrons, conductive flux, and coronal pressure. *ApJ* **282**, 296–307 (1984).
38. Canfield, R. C. & Gayley, K. G. Impulsive H-alpha diagnostics of electron-beam-heated solar flare model chromospheres. *ApJ* **322**, 999–1009 (1987).
39. De Pontieu, B. *et al.* The Interface Region Imaging Spectrograph (IRIS) **289**, 2733–2779 (2014).
40. Lemen, J. R. *et al.* The Atmospheric Imaging Assembly (AIA) on the Solar Dynamics Observatory (SDO). *SoPh* 241–+ (2011).
41. Scharmer, G. B., Dettori, P. M., Lofdahl, M. G. & Shand, M. Adaptive optics system for the new Swedish solar telescope. In Keil, S. L. & Avakyan, S. V. (eds.) *Innovative Telescopes and Instrumentation for Solar Astrophysics*, vol. 4853 of *Society of Photo-Optical Instrumentation Engineers (SPIE) Conference Series*, 370–380 (2003).
42. Scharmer, G. B. Comments on the optimization of high resolution Fabry-Pérot filtergraphs. *A&A* **447**, 1111–1120 (2006).
43. Scharmer, G. B. *et al.* CRISP Spectropolarimetric Imaging of Penumbra Fine Structure. *ApJL* **689**, L69–L72 (2008).
44. Heinzel, P. & Kleint, L. Hydrogen Balmer Continuum in Solar Flares Detected by the Interface Region Imaging Spectrograph (IRIS). *ApJL* **794**, L23 (2014).
45. Kleint, L. *et al.* Detection of Supersonic Downflows and Associated Heating Events in the Transition Region above Sunspots. *ApJL* **789**, L42 (2014).
46. Kuridze, D. *et al.* H α Line Profile Asymmetries and the Chromospheric Flare Velocity Field. *ApJ* **813**, 125 (2015).
47. Rubio da Costa, F., Kleint, L., Petrosian, V., Liu, W. & Allred, J. C. Data-driven Radiative Hydrodynamic Modeling of the 2014 March 29 X1.0 Solar Flare. *ApJ* **827**, 38 (2016).
48. Aboudarham, J. & Henoux, J. C. Non-thermal excitation and ionization of hydrogen in solar flares. I - Effects on a flaring chromosphere. *A&A* **168**, 301–307 (1986).
49. Zharkova, V. V. & Kobylinskii, V. A. The effect of non-thermal excitation and ionization on the hydrogen emission in impulsive solar flares. *SoPh* **143**, 259–274 (1993).
50. Zharkov, S., Green, L. M., Matthews, S. A. & Zharkova, V. V. 2011 February 15: Sunchokes Produced by Flux Rope Eruption. *ApJL* **741**, L35 (2011).
51. Zharkova, V. & Zharkov, S. On the Generation of Hydrodynamic Shocks by Mixed Beams and Occurrence of Sunchokes in Flares. *SoPh* **290**, 3163–3188 (2015).
52. Moore, R. L. & Datlowe, D. W. Heating and cooling of the thermal X-ray plasma in solar flares. *SoPh* **43**, 189–209 (1975).
53. Antiochos, S. K. Radiative-dominated cooling of the flare corona and transition region. *ApJ* **241**, 385–393 (1980).

54. Tritschler, A. *et al.* DKIST: Observing the Sun at High Resolution. In van Belle, G. T. & Harris, H. C. (eds.) *18th Cambridge Workshop on Cool Stars, Stellar Systems, and the Sun*, vol. 18 of *Cambridge Workshop on Cool Stars, Stellar Systems, and the Sun*, 933–944 (2015).
55. van Noort, M., Rouppe van der Voort, L. & Löfdahl, M. G. Solar Image Restoration By Use Of Multi-frame Blind De-convolution With Multiple Objects And Phase Diversity. *SoPh* **228**, 191–215 (2005).
56. de la Cruz Rodríguez, J., Löfdahl, M. G., Sütterlin, P., Hillberg, T. & Rouppe van der Voort, L. CRISPRED: A data pipeline for the CRISP imaging spectropolarimeter. *A&A* **573**, A40 (2015).
57. Somov, B. V., Sermulina, B. J. & Spektor, A. R. Hydrodynamic response of the solar chromosphere to an elementary flare burst. II - Thermal model. *SoPh* **81**, 281–292 (1982).
58. Zharkova, V. V. & Gordovskyy, M. The Effect of the Electric Field Induced by Precipitating Electron Beams on Hard X-Ray Photon and Mean Electron Spectra. *ApJ* **651**, 553–565 (2006).
59. Boerner, P. *et al.* Initial Calibration of the Atmospheric Imaging Assembly (AIA) on the Solar Dynamics Observatory (SDO). *SoPh* **275**, 41–66 (2012).
60. Dobranskis, R. R. & Zharkova, V. V. Updated analytical solutions of continuity equation for electron beams precipitation - I. Pure collisional and pure ohmic energy losses. *MNRAS* **453**, 229–241 (2015).
61. Zharkova, V. V. & Kobylinskii, V. A. Investigation of Nonthermal Excitation and Ionization of Hydrogen in Low-Temperature Flare Plasma - Part Two - Computational Method. *Soviet Astronomy Letters* **17**, 34–+ (1991).
62. Ding, M. D. & Fang, C. H α Emission Line Profiles of Solar Flares with Turbulent Velocity Fields. *SoPh* **147**, 305–321 (1993).
63. Ivanov, V. V. & Serbin, V. M. The transfer of line radiation. I - General analysis of approximate solutions. *Soviet Ast.* **28**, 405–409 (1984).

5. ACKNOWLEDGEMENTS

MD and VZ wish to acknowledge the PhD studentship support from Northumbria University via the University Research Development Fund at Research Councils UK (RCUK). The authors are most grateful to the staff of the SST for their invaluable support with the observations. The Swedish 1-m Solar Telescope is operated on the island of La Palma by the Institute for Solar Physics at Stockholm University in the Spanish Observatorio del Roque de los Muchachos of the Instituto de Astrofísica de Canarias.

6. AUTHOR CONTRIBUTIONS

Malcolm Druett: Calculations of NLTE model and theoretical line profiles and light curves, reduction of observational profiles, comparison of the profiles with simulations, producing figures, writing the paper and its discussion.

Eamon Scullion: Interpretation and analysis of observations from SDO and SST, editing and discussion of the paper.

Valentina Zharkova: formulation of the NLTE and hydrodynamic problems, hydrodynamic and NLTE simulations, writing the paper, editing and discussion.

Sarah Matthews: processing of RHESSI data, building the energy spectra for this event and beam parameters, paper editing and discussion.

Sergei Zharkov: reduction of HMI magnetic data, producing plots for Fig. 1, investigation of HMI helioseismic data for this event, hydrodynamic simulations, paper editing and discussion.

Luc Ruppe Van Der Voort: Observer and provided observational data reduction for SST.

7. ADDITIONAL INFORMATION

The authors declare that there are no conflicts of interest regarding the publication or research contained within this work.

The authors declare no competing financial interests.

8. FIGURE CAPTIONS

8.1. Figure 1

The active region topology and HXR emission. (a) The GOES X-Ray light curves of the flare in the 1–8 Å (black) and 0.5–4.0 Å (magenta) channels. The vertical dashed lines correspond to the time interval of the RHESSI spectrum in event 2. (b) RHESSI photon flux spectrum for event 2 with residuals derived with CLEAN in the 20 s interval around the time of H α emission for thermal (green line) plus single power-law (yellow line) components, giving the total (magenta line). HXR emission is mostly of thermal nature with a small non-thermal component (see for details the current section and 'Methods section: Reduction of H α line emission') with the parameters: spectral index about 3.8 and initial energy flux can be a factor (0.7–3) of $F_0 = 10^{10}$ erg-cm $^{-2}$ ·s $^{-1}$. (c) The HXR emission contours appearing in event 1 (top) and event 2 (Bottom, blue contour) coinciding with the times of the observations of H α kernels with

red-shifts in the ribbon (09:16 UT). These are overlaid onto the HMI magnetogram. The response in the 5-12 keV channel is shown using red contours, and the response in the 12-25 keV channel with blue. (d) HXR emission overlaid on the HMI magnetogram appearing with the event 3 occurring ~ 4 minutes later (09:20 UT), during the maximum in GOES light curve.

8.2. Figure 2

Observations with AIA. (a) *Background*: A context image for the observation in AIA 193 Å overlaid with the CRISP FOV outlined in green within AR11778. *Inset left*: The co-temporal (09:16:09 UT) CRISP image in the H α line far red wing reveals bright flare ribbons point to by the white arrow for event 2 that are co-spatial within RHESSI imaging contours in 6-12 keV (green) and 12-25 keV (purple). *Inset right*: The H α dopplergram for the 33 pt. spectral scan per pixel, containing blue/red-shifted motions marked by the relevant colour presented in the range of ± 20 km·s $^{-1}$. The blue boxes in the insets (a) highlight the section of the ribbon formation in event 2, which is displayed in panel (b). (b) The image sequence describing evolution of the ribbon in the AIA 94 Å, 171 Å and 304 Å channels from top to bottom, respectively. These are co-spatial and co-temporal with the bright ribbon features (contoured in red), in the H α far red-wing images of +1.3 Å (bottom panel). The 171 Å channel reveals a bright jet-like protrusion (within the blue boxed region) that appears to form between the time frames 09:15:54 UT +15 s and +29 s (corresponding to 93 km·s $^{-1}$) in the direction of the blue arrow and disappears by the time frame +49 s.

8.3. Figure 3

H α line profile observations using SST. (a) The CRISP H α line core image (6563 Å) with a blue box outlining the part of the flare ribbon under investigation. The green box corresponds to the pixels selected to construct the average quiet Sun spectral profiles, i.e. close to the ribbon formation and free of any activity, within the time interval of the ribbon formation. (b) The corresponding FOV for the H α far red wing intensity at +1.3 Å, with a red box corresponding to the region where the spectral profiles of interest are extracted. (c) The contoured ribbons of the H α line core image for the blue box region is presented. (d) The averaged and normalized H α spectral line profiles, determined from the red box pixels, are presented for time intervals corresponding to the 1st (09:15:54 UT: red solid line), the 2nd (+7 s: purple solid line) and the 3rd (+16 s: blue solid line) time frames. The H α line profiles display exceptionally strong red-shifts. (e) The averaged and normalized H α spectral line profiles for significantly later time frames corresponding to +29 s (red solid line), +49 s (purple solid line) and +56 s (blue solid line) when there were no longer strong red-shifts but rather core emission with peaks in both blue and red near wings. The black solid lines describes the averaged QS background H α profile, deduced from the region defined by the green box in (a). Intensities were normalised against the background levels using the QS intensity of 9890 counts per pixel at 6561.7 Å as a reference.

8.4. Figure 4

Simulated hydrodynamic responses. The simulated hydrodynamic responses of a flaring atmosphere to injection of a beam with the initial flux of 10^{10} erg·cm $^{-2}$ ·s $^{-1}$ (F10 model, left panels) and 3×10^{10} erg·cm $^{-2}$ ·s $^{-1}$ (3F10 model, right panels) following Zharkova & Zharkov²³ showing column depth dependencies of: (a and d) - the electron kinetic temperature, K, (b and e) - the plasma macrovelocity, km·s $^{-1}$, and (c and f) - the plasma number density, cm $^{-3}$ forming a flaring corona, chromosphere and photosphere (see the text for more details).

8.5. Figure 5

Simulated and observed H α line enhancements. (a) the synthetic H α line normalised intensity versus a distance $(\lambda - \lambda_0)$, in Å, from the H α line central wavelength, λ_0 ($\lambda_0 = 6563$ Å) taken from the simulation at +5 s after a beam onset for the F10 model (magenta line), the 3F10 model (cyan line) and a model with initial flux 7×10^9 erg·cm $^{-2}$ ·s $^{-1}$ (7F9 model, yellow line) (b) the normalised background-subtracted H α profile observed +7 s after the ribbon onset in the event 2. (c) The H α line normalised intensity simulated for the F10 model at later times after the beam onset: +30 s (red solid line) and +70 s (blue solid line) and (d) the observed H α profiles at the similar times of +29 s (red solid line) and +56 s (blue solid line) after the event 2 onset.

8.6. Figure 6

The normalised response functions of the AIA channels. The normalised response functions of the AIA 94 Å (green line), 171 Å (yellow line) and 304 Å (red line) channels plotted against \log_{10} of T (temperature). The AIA 94 Å channel has its largest sensitivity peak close to 10 MK but it is not limited in sensitivity to that specific temperature. It is shown in the green line that the AIA 94 Å channel has a secondary peak with maximum at the temperature of 1-2 MK.

8.7. *Figure 7*

Simulated and observed AIA light curves. (a) The simulated light curves in the AIA 94 Å (green line) and 171 Å (yellow line) channels for contributions from the flaring corona, transition region and chromosphere. The simulation does not include background from the overlying upper corona or neighbouring corona. Observed values for the 94 Å (green crosses) and 171 Å (yellow crosses) channels including this background are shown. (b) The simulated profiles of the signals in AIA 94 Å (green line) and 171 Å (yellow line) above background. These profiles have been normalised to 1 at their peak values. The AIA 171 Å channel is particularly bright compared to the AIA 94 Å channel at around 30 s. (c) The normalised fractional excess in AIA 171 Å. The normalised light curves in panel b were subtracted to find the relative excess in the 171 Å channel. This excess is plotted as a fraction of the emission in the 171 Å channel at each instant. The full width half maximum (Horizontal black bar) indicates the times at which the jet is particularly bright in AIA 171 Å compared to AIA 94 Å, the vertical bar represents the maximum relative brightness at around 30 s.